Photovoltaic performance of magnetron sputtered antimony selenide thin film solar cells buffered by cadmium sulfide and cadmium sulfide /zinc sulfide

Ayten Cantas [a,*], S. Hazal Gundogan [b], Fulya Turkoglu [c,d], Hasan Koseoglu [d], Gulnur Aygun [b], Lutfi Ozyuzer [b,e]

[a] Department of Electric and Energy, Pamukkale University, Kınıklı, Denizli 20160, Turkey
[b] Department of Physics, Izmir Institute of Technology, Urla, Izmir 35430, Turkey
[c] Department of Metallurgical and Materials Engineering, Iskenderun Technical University, Iskenderun, 31200, Hatay, Turkey
[d] ISTE Center for Science and Technology Studies and Research (ISTE-CSTSR), Iskenderun Technical University, Iskenderun, Hatay 31200, Turkey
[e] Teknoma Technological Materials Ltd., IZTEKGEB, IYTE Campus, Urla, Izmir 35430, Turkey

ARTICLE INFO

ABSTRACT

Antimony selenide (Sb_2Se_3)-based thin-film solar cells have recently attracted worldwide attention as an abundant, low-cost, and efficient photovoltaic technology. The highest efficiencies recorded for Sb_2Se_3 solar cells have been obtained using cadmium sulfide (CdS) as a buffer layer. The Cd-included hybrid buffer layers could be one option to increase device efficiency through more effective usage of light. Therefore, in this work, the effect of single CdS and hybrid CdS/zinc sulfide (ZnS) buffer layers on the photovoltaic performance of Sb_2Se_3 thin-film solar cells has been investigated in detail. Sb_2Se_3 thin films have been deposited on molybdenum (Mo)-coated soda-lime glass (SLG) substrates by radio frequency magnetron sputtering technique followed by a post-heat treatment process. The morphological, and structural properties of Sb_2Se_3 thin films have been investigated by X-Ray Diffraction and Scanning Electron Microscopy. To compare the device performances of single CdS and hybrid CdS/ZnS buffered Sb_2Se_3 thin-film solar cells, SLG/Mo/Sb_2Se_3/CdS/ZnS/indium tin oxide (ITO) and SLG/Mo/Sb_2Se_3/CdS/ITO structures have been fabricated. The findings of this study have revealed a reduction in solar cells' performance from η=3.93% for CdS buffer to η=0.13% for CdS/ZnS hybrid buffer. The change in the solar cell performance using the CdS/ZnS hybrid buffer has been discussed in detail.

1. Introduction

Energy, which is an important component of social and economic development, has become a global crisis due to the decrease in fossil resources. Reliable and sustainable sources are required to be developed more to solve this energy crisis. Photovoltaic technologies have been identified as an applicable alternative to overcome the energy shortage problem. Compound thin-film solar cells have recently become a hot research topic due to their low material waste and low energy consumption. The current popular compound thin-film solar cells are cadmium telluride (CdTe), copper indium gallium selenide (CIGS), and copper zinc tin selenide with efficiencies of 22.1%, 23.35%, and 12.6%, respectively [1,2]. As a recent addition to the thin-film photovoltaic family, antimony selenide (Sb_2Se_3) is one of the most promising

absorber material choices among the inorganic semiconductors. Besides having nontoxic, earth-abundant, and low-cost elements, it has an optical bandgap of 1.2eV, a high absorption coefficient ($>10^5$ cm^{-1}), moderate carrier mobility (10 cm^2 V^{-1} s^{-1}), long carrier lifetime (60ns) and a low cost [3–5]. In 2009, a Sb_2Se_3-based thin-film solar cell was fabricated by Messina et al. using a chemical bath deposition (CBD) technique, and 0.66% photoconversion efficiency (PCE) was achieved [6]. In a short period, the efficiency of Sb_2Se_3-based solar cells prepared by spin coating was increased to 2.26% [7]. In 2018, 7.6% efficiency was recorded by Wen et al. for the Sb_2Se_3-based solar cell in superstrate configuration deposited using the vapor deposition technique [8]. After intensive studies, in just 10 years, Sb_2Se_3 in the substrate structure has shown very rapid growth, reaching 9.2% PCE. [9]. Although theoretical calculations show that more efficient Sb_2Se_3 solar cells are possible, to

---

date, the achievable efficiencies of antimony chalcogenides solar cells are largely suppressed due to the open-circuit voltage (V_{OC}) deficiency. For Sb_2Se_3 solar cells, the large V_{OC} loss has been generally attributed to bulk defects, impurities in bulk, and interfacial trap states [10,11]. It is very difficult to prevent the formation of these defects and interfacial trap states by controlling the growth parameters alone. To reduce the V_{OC} loss, both optimization of material and regulation of device structure might be considered. For Sb_2Se_3 thin-film solar cells, the traditional device structure is Soda-lime glass (SLG)/Molybdenum (Mo)/Sb_2Se_3/-Cadmium sulfide (CdS)/Zinc oxide (ZnO)/Indium tin oxide (ITO). However, the short-wavelength response of Sb_2Se_3 is limited by the loss of carrier collection due to the narrow bandgap (2.42eV) of CdS [12]. The structure of band alignment at the heterojunction is also another important factor that affects the interface recombination. Sb_2Se_3/CdS interface has a cliff-type band alignment that can increase the interface recombination and reduce V_{OC}. In the literature, hybrid buffer layers have been developed as an alternative to single CdS buffers such as Indium sulfide (In_2S_3) /CdS, Zinc sulfide (ZnS)/CdS, and Zinc oxysulfide (Zn(O,S))/CdS [12–14].

Hybrid buffer can reduce the recombination paths at the heterojunction interface and lead to an increase in the V_{OC} [15]. However, although there are many theoretical studies on hybrid buffered thin-film solar cells in the literature [12–14,16], experimental studies on this subject are limited. Among to proposed hybrid buffers, exploring ZnS/CdS to improve device performance may be an option, since ZnS having a band gap of 3.5–3.8eV allows more high-energy photons to penetrate the buffer and hereby the junction between absorber and buffer [16]. The effect of the ZnS/CdS hybrid buffer layer on the performance of Sb_2Se_3-based solar cells was studied theoretically by Maurya et al. They claimed that using a ZnS/CdS hybrid buffer layer can improve the Sb_2Se_3-based solar cell performance by up to 22.22% which is higher than the efficiency of a cell with a single buffer layer of CdS or ZnS [17]. Mohamed et al. reported a theoretical study on ZnS/CdS hybrid for CdTe thin-film solar cells having ITO/ZnS/CdS/CdTe structure. In this work, the total thickness of the ZnS/CdS hybrid buffer was kept constant at 60nm and the thickness of ZnS was varied from 0 to 60nm. They found that the increase in the ZnS thickness up to 30nm resulted in the reduction of absorption losses and an increment in the photoconversion efficiency of CdTe solar cells [18]. The other numerical study investigating the effect of a hybrid buffer layer on copper zinc tin sulfide (CZTS) solar cells was reported by Tripathi et al. [19]. The thickness of CdS was kept constant in CZTS/CdS/ZnS/Aluminum-doped Zinc Oxide solar cell structure, and the variation of efficiency with respect to ZnS thickness was investigated. It was observed that the efficiency decreased as the ZnS thickness increased for each fixed thickness of the CdS buffer layer. So far, the mentioned hybrid buffer layer modifications have been studied experimentally for only CIGS [12,16, 20], and CZTS-based solar cells [21]. Garris et al. investigated the photovoltaic performance of CIGS solar cells with CdS, Zn(O,S), and CdS/Zn(O,S) buffers. The solar cell with a single Zn(O,S) buffer exhibited poor device properties when compared with the cells with CdS and CdS/Zn(O,S) buffers. They claimed that, when CdS was involved in the cell structure, in either CdS or CdS/Zn(O,S) buffer layers, the devices were better than Zn(O,S) alone, which suggests that CdS makes the device better. Solar cells with thin CdS following Zn(O,S) deposition exhibited equal or better device performance than CdS alone [20]. Rana et al. fabricated CIGS solar cells with various buffers including CdS, CdS-treated, Zn(O,S), CdS/Zn(O,S), and CdS-treated/Zn(O,S). They obtained their best results for the cell with CdS buffer. However, the solar cell with CdS-treated/Zn(O,S) showed comparable performance to the best cell. This cell also exhibited better performance than the cells with Zn(O,S) and CdS/Zn(O,S) [12]. CdS and double buffer layer (ZnS/CdS) CIGS solar cells with and without a single i-ZnO layer were prepared by Ho et al.

In this work, the deposition time of CdS was kept constant at 5min, whereas ZnS was varied from 5min to 15min. The results demonstrated that ZnS/CdS double buffer layer can omit the i-ZnO and the best photovoltaic performance was achieved for the cell with double buffer (ZnS-10min/CdS-5min) [16]. Yan et al. investigated the photovoltaic performance of CZTS solar cells using In_2S_3, CdS, In_2S_3/CdS, and CdS/In_2S_3 buffer layers. When compared to a single CdS buffered CZTS cell, they achieved a substantial boost in the Voc using single In_2S_3 and In_2S_3/CdS hybrid buffers. In the case of a CZTS device with a hybrid buffer of CdS/In_2S_3, although V_{OC} improved, both the fill factor (FF) and short circuit current density (Jsc) dropped, leading to a decreased efficiency [21].

The main intention of this study is to investigate the variation of the photovoltaic response of Sb_2Se_3 thin-film solar cells in the case of a CdS/ZnS hybrid buffer layer experimentally. In this study, SLG/Mo/Sb_2Se_3/CdS/ZnS/ITO and SLG/Mo/Sb_2Se_3/CdS/ITO structures were fabricated and performances of single CdS and hybrid CdS/ZnS buffered Sb_2Se_3 thin-film solar cells were compared. Morphological and structural properties of Sb_2Se_3 thin-film fabricated by magnetron sputtering technique were also investigated. The findings of this work provide relevant information on how single CdS and hybrid CdS/ZnS buffer layers affect the overall performance of the Sb_2Se_3 thin-film solar cells.

2. Experimental

2.1. Absorber layer deposition

Sb_2Se_3 absorber films were deposited using a two-step process on SLG and 1μm thick Mo-coated SLG substrates. The commercially purchased rectangular shape SLGs (Thermo Scientific) with 1.1mm thick and 25×10 mm^2 surface area were used as substrates. Before the deposition, all substrates were cleaned by ultrasonication in acetone, ethanol, and distilled water for 5 min in each process, and then exposed to nitrogen plasma for 15 min at 100W RF bias. Coating of films was performed by radio frequency (RF) magnetron sputtering technique at room temperature. A disk-shaped antimony selenide target (Testbourne) having 99.999% purity with a 5.1mm diameter and 0.64mm thickness was used as a sputtering target. The distance between the target and substrate was fixed at 8cm. Prior to the deposition process, the sputtering chamber was evacuated below 1.99×10^{-4}Pa vacuum level using a turbo molecular pump and rough pump.

The RF power was set to 30W, 30 standard cubic centimeters per minute (sccm) Ar was used as sputtering gas and the operating pressure was approximately 0.16Pa during the deposition. Before the deposition process, the shutter was set in a closed position for the pre-sputtering process to clean the target surface from possible contaminations. After opening the shutter, deposition occurred for 30min. Through several calibration runs, the thickness of the films deposited for 30min on SLG substrates was determined as 500nm using a Dektak profilometer. After the deposition process, the prepared samples were annealed in a 70cm long quartz tube integrated into a tubular furnace under 100 sccm Ar flow. The temperature ramping rate, the annealing temperature, and the annealing duration parameters were set as 20°C/min, 350 °C, and 30min, respectively. After the annealing process, films were left naturally cooling. The crystal structure of SLG/Mo/Sb_2Se_3 layer stacks was characterized by X-ray diffraction (Marvel Panalytical Empyrean XRD) operated in the Bragg–Brentano focusing geometry from 10° to 55° with Cu Kα radiation source ($\lambda = 1.5406$Å) using a step size of 0.03° and a step time of 1.1s. The surface morphology and composition of the SLG/Sb_2Se_3 layer were investigated by FEI-QuantaFEG 250 Scanning Electron Microscopy (SEM) and Oxford X-act Energy Dispersive X-Ray Spectroscopy (EDS) integrated into FEI-QuantaFEG 250 SEM, respectively. Surface topography was imaged with 7kV acceleration voltage at 10000X magnification under high vacuum with the Everhart-Thornley detector and 3.0 spot size. The EDS analysis was carried out at 1000X magnification using a backscattered electron detector, HV resolution (20kV), and 5.0 spot size in a high vacuum. For the microstructural characterization, a high-resolution confocal micro-Raman spectroscopy

(S&I, MonoVista, employing Princeton Instruments, Acton SP2750 0.750m Imaging Triple Grating Monochrometer) was used in the back-scattering geometry with a spectral resolution of about 1 cm^{-1} at room temperature. To analyze the compositional structure of the SLG/Mo/Sb$_2$Se$_3$ layer stack, an argon ion laser operating at 514nm (100mW) was used as the Raman excitation source. 100X objective giving spot size near 3μm in diameter was used and the spectral data were collected with a CCD detector at about 0.5 cm^{-1} max resolution in the visible. A rough scan was carried out using a 150 gr/mm grating first then a high-resolution measurement followed by a 600 gr/mm grating. X-ray photoelectron spectroscopy (XPS; SPECS Phoibos 150 3D-DLD) was used to identify the core electronic states and hence, the number of constituent elements. XPS measurement of the Sb$_2$Se$_3$ film was performed with a non-monochromatic Mg Kα radiation source (hν = 1254eV) with a power of 150W and a take-off angle of 45° The analyzer pass energy, step size, dwell time, and spot size were set to 30eV, 0.05eV, 2s, and 2mm, respectively, for high-resolution spectra of Sb *3d*, Sb *4d*, and Se *3d* valence regions. A PerkinElmer Lambda 950 UV/VIS/NIR spectrometer was used for transmission measurement. The electrical properties of the film were studied by Hall-effect Measurement System (NanoMagnetic instruments ezHEMS system) using the Van der Pauw technique at room temperature.

2.2. Buffer layer deposition

An n-type semiconductor CdS was used as a buffer layer. 50nm thick CdS layer was deposited using the CBD technique. Since it is difficult to deposit a uniform and pinhole-free CdS layer less than 50nm thick by a CBD technique, the thickness of CdS was kept constant at 50nm for both device structures.

In order to determine the elemental composition and vibration modes and to characterize the optical and electrical properties of CdS film, it was deposited on an SLG substrate by the chemical bath deposition technique. The SLG substrate was cleaned by ultrasonication in acetone, ethanol, and distilled water, respectively, and then dried under a nitrogen stream. For the preparation of bath solution, 1.2ml of 0.5M cadmium acetate (Cd(CH$_3$CO$_2$)$_2$), 6ml of 2M ammonium acetate (NH$_4$CH$_3$CO$_2$), 7ml of 0.5M thiourea SC(NH$_2$)$_2$, and 12ml of 14.4M (25% of NH$_3$ solution) ammonium hydroxide (NH$_4$OH) were added to the 270ml de-ionized water. In this bath solution, cadmium acetate and thiourea were used as the cadmium and sulfur sources, respectively while NH$_3$ had a role as a complexing agent to prevent metal hydroxide precipitation. During the deposition, the bath solution was stirred at a constant speed with the aid of a magnetic stirrer, and the pH value of the solution was changed from 9 to 11. The CdS thin film was deposited at 85°C for 20min. After the deposition process, the substrate was first rinsed with deionized water at a temperature of 60°C in order to remove CdS precipitation or un-reacted sulfide ions and then rinsed again with deionized water at room temperature and dried in air. The grown film was light yellow in color and displayed well adherence to the SLG surface.

The other n-type semiconductor that is used as a second buffer layer is ZnS. 50nm thick ZnS was deposited on SLG/Mo/Sb$_2$Se$_3$/CdS layer stack by RF magnetron sputtering method using a disk-shaped ZnS sputtering target (Kurt J. Lesker) having 99.99% purity with a 5.1mm diameter and 0.64mm thickness. Before the deposition, the sputtering system was evacuated up to 2.66 × 10^{-4}Pa base pressure, and during the deposition, 40W RF power, 50 sccm Ar gas, and 8cm target to substrate distance were used.

The thickness of the CdS and ZnS films was determined as approximately 50nm using a Veeco DEKTAK 150 profilometer. The surface morphology of grown CdS film was investigated using a Scanning Electron Microscope (FEI-QuantaFEG 250) by using 5kV acceleration voltage, at 100000X magnification under high vacuum with the Everhart-Thornley detector and 3.0 spot size. To obtain information about the stoichiometry of the CdS and ZnS films, the Energy Dispersive

Spectroscopy (Oxford X-act) analysis was carried out at 1000X magnification using a backscattered electron detector, HV resolution (10kV), and 3.0 spot size in a high vacuum. Raman analysis of CdS and ZnS thin films was investigated using a high-resolution confocal micro-Raman spectroscopy (S&I, MonoVista, employing Princeton Instruments, Acton SP2750 0.750m Imaging Triple Grating Monochrometer) in the back-scattering geometry with a spectral resolution of about 1 cm^{-1} at room temperature. The measurements were performed using an excitation source operating at 488nm wavelength. 100X objective giving spot size near 3μm in diameter was used and the spectral data were collected with a CCD detector at about 0.5 cm^{-1} max resolution in the visible. A high-resolution scan was carried out using a 600 gr/mm grating. Optical transmission measurement which was used for optical bandgap calculation was employed in the range of 200–2600nm at room temperature using a PerkinElmer Lambda 950 UV/VIS/NIR spectrometer. Electrical characteristics of CdS and ZnS thin films were determined by Hall measurements taken at room temperature using ezHEMS (NanoMagnetic) instrument.

2.3. Solar cell device fabrication

200nm thick ITO window layer was coated on deposited buffer layers by direct current (DC) magnetron sputtering technique using a disk shape indium doped tin oxide target (Testbourne) having 99.99% purity with a 5.1mm diameter and 0.64mm thickness, 15-Watt DC power, and 40 sccm argon flow under 0.13Pa operation pressure. Sb$_2$Se$_3$-based solar cells were fabricated in two device structures as given in Fig. 1 (a,b). The solar cells grown in the SLG/Mo/Sb$_2$Se$_3$/CdS/ZnS/ITO and SLG/Mo/Sb$_2$Se$_3$/CdS/ITO configurations were named with cell-1 and cell-2, respectively. After the deposition of the ITO layer, the cell active area was defined out of a large area of the Sb$_2$Se$_3$ solar cell stack by removing the layers on top of Mo outside the cell area. Finally, the cells were directly contacted with silver epoxy via the window layer for photovoltaic characterization. The cross-section view of the solar cells was
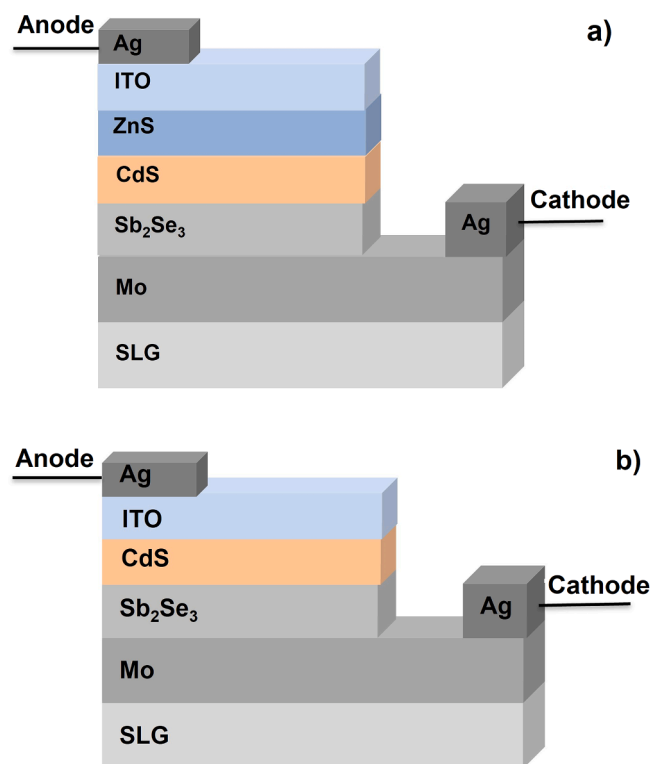

Fig. 1. The device structure of Sb$_2$Se$_3$-based thin-film solar cells (a) with a hybrid CdS/ZnS buffer layer, and (b) with a single CdS buffer layer.

monitored by Thermo Fisher Scientific Apreo S LoVac Scanning Electron Microscope using 10kV acceleration voltage at 50000X magnification under high vacuum with the Everhart-Thornley detector and 8.0 spot size. The device performance of the Sb_2Se_3-based solar cells was investigated using a current-voltage (I-V) measurement system under dark and illuminated conditions. Since the solar cells have been fabricated in the substrate configuration, the top of the cell (ITO side) was illuminated. I-V curves were measured using a multimeter (Keithley, 2000 Series) under AM 1.5G light illumination from a solar simulator (Abet Technologies' model 11,002 SunLite) with intensity calibrated to 100mW/cm^2 through a Si reference cell. The voltage was forwardly and backwardly scanned from −1V to 1V with a scan rate of 0.01V/s.

3. Results and discussions

3.1. Analysis of Sb$_2$Se$_3$ thin film

3.1.1. Crystal structure of Sb$_2$Se$_3$ thin film

Fig. 2 represents the X-ray diffraction pattern of the Sb_2Se_3 thin film. The film showed the polycrystalline structure and exhibited characteristic peaks of the Sb_2Se_3. The XRD pattern of the film matched well with the orthorhombic structure of Sb_2Se_3 (JCPDS 15–0861). The (020), (120), and (130) diffraction peaks were observed stronger than other peaks in the XRD pattern, hinting that the sample had a [hk0] preferred orientation. Moreover, a signal from Mo back contact was observed at 40.5° (110) [22]. The XRD pattern also exhibited the main diffraction peak of Se at 43.18° through the (101) plane (JCPDS 96–901–3132). The interplanar spacing (d_{hkl}) of the diffraction plane was calculated from Bragg's law as given by Eq. (1) [23]. It is well known that the relationship between lattice constants (a,b,c) and d_{hkl} is given by Eq. (2) for an orthorhombic crystal structure [24,25].

$$n\lambda = 2d\sin\theta \tag{1}$$

$$\frac{1}{d_{hkl}^2} = \frac{h^2}{a^2} + \frac{k^2}{b^2} + \frac{l^2}{c^2} \tag{2}$$

Here, h, k, and l are the Miller indices of the diffraction plane, λ is the wavelength of the Cu-$K\alpha$ line ($\lambda = 0.15406$nm), n is an integer that refers to the "order" of reflection, and θ is the Bragg angle in degrees. The lattice parameters were calculated using the first-order reflection on the (020), (120), and (221) planes. The lattice parameters a, b, and c were obtained as 11.68 Å, 11.82 Å, and 3.98 Å, respectively. These values are close to the standard cell parameters a=11.63 Å, b=11.78 Å, and c=3.99 Å as given in the Joint Committee on Powder Diffraction Standards (JCPDS) 15–0861 document.

3.1.2. SEM and EDS analysis of Sb$_2$Se$_3$
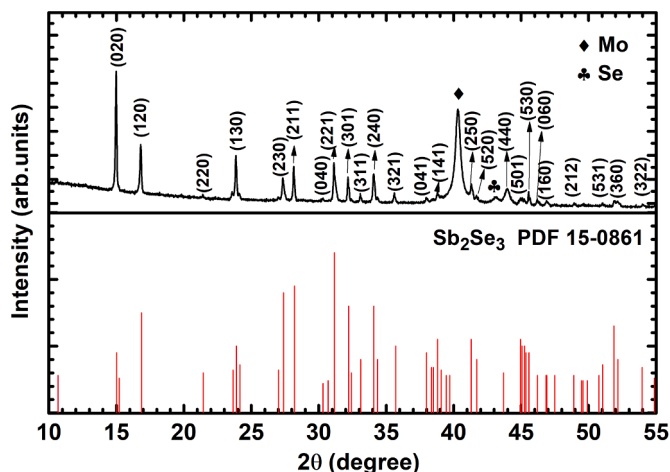
The two-dimensional topographical image obtained from the Sb_2Se_3 film on the SLG substrate was shown in Fig. 3 (a). The Sb_2Se_3 film was nearly featureless which indicates that the film was amorphous. It was seen that the sputtered Sb_2Se_3 film covers the substrate surface very well. The chemical composition result of the Sb_2Se_3 thin film was analyzed by energy-dispersive X-Ray spectroscopy, which is given in Fig. 3 (b). Based on the inset table in Fig. 3 (b), the Sb_2Se_3 film was nearly stoichiometric with Sb/Se ratio is 0.64. EDS measurements were performed for approximately 20 fabricated Sb_2Se_3 thin films. Since the single target of Sb_2Se_3 was used during sputtering, all EDS results had very close values.

3.1.3. Raman analysis of Sb$_2$Se$_3$

The vibration modes in the Sb_2Se_3 film and its impurity phases were described using Raman spectroscopy. It is known that Sb_2Se_3 has 60 zone center phonons of symmetry Γ=10A$_g$ + 5B$_{1g}$ + 10B$_{2g}$ + 5B$_{3g}$ + 5A$_u$ + 10B$_{1u}$ + 5B$_{2u}$ + 10B$_{3u}$. Modes of A exhibit symmetric behavior, whereas modes of B are anti-symmetric. Since the A$_u$ modes are silent and the B$_u$ modes are IR-active, the Raman active modes of the Sb_2Se_3 are A$_g$, B$_{1g}$, B$_{2g}$, and B$_{3g}$ [26]. In our case, the Raman spectra in Fig. 4 display peaks at about 100, 117, 134, 162, 210, 240, and 254 cm^{-1}. The main band detected at 210 cm^{-1} is commonly reported for A$_{1g}$ mode of Sb-Se-Sb bending vibration in Sb_2Se_3 [27]. Since the broad nature and low intensity of the features in the region from 90 to 180 cm^{-1}, it was difficult to identify the vibration modes exactly. In this region, the broad bands at around 100, 117, and 134 cm^{-1} were attributed to the A$_g$ vibration modes of orthorhombic Sb_2Se_3 [26]. The second intense vibration peak that appeared at 254 cm^{-1} was commonly reported to be related to the Se$_6$ rings or the Sb_2O_3 phase [27]. For our film, this vibration mode might be assigned to both phases. The unresolved peak detected at approximately 240 cm^{-1} could be also considered a trigonal Se$_8$ ring [25,28–30]. Trigonal selenium is the most stable phase of

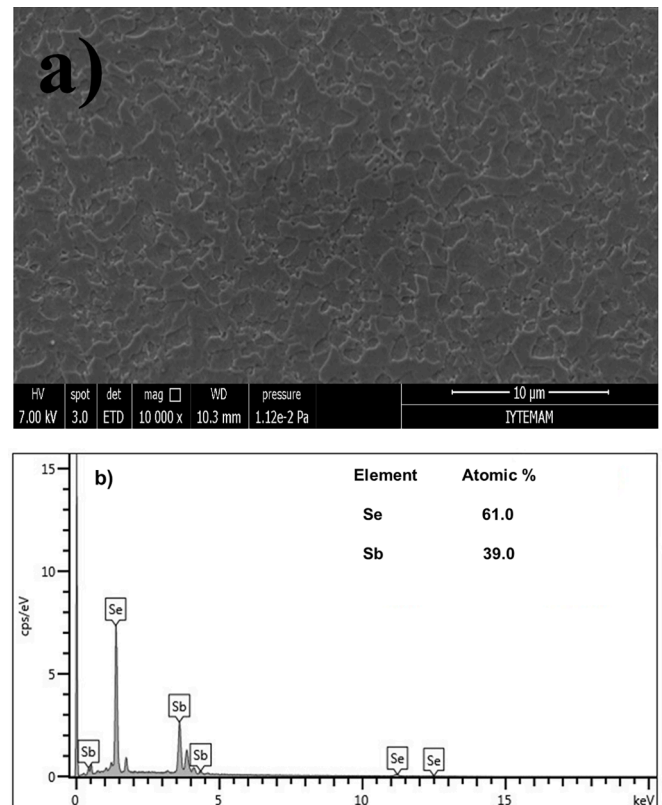**Fig. 2.** XRD pattern of Sb$_2$Se$_3$ thin film deposited on Mo-coated SLG substrate.

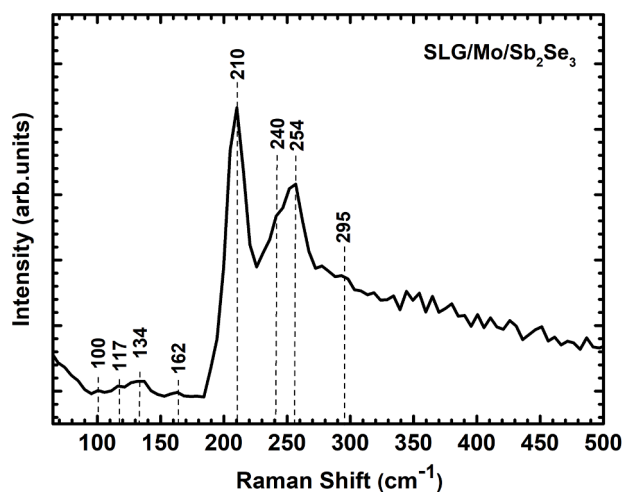**Fig. 3.** Sb$_2$Se$_3$ film on SLG substrate a) surface topography and b) EDS analysis.

Fig. 4. Raman analysis of Sb_2Se_3 thin film deposited on Mo coated SLG substrate.

selenium. The existence of this peak is consistent with the slightly selenium-rich composition of the film which was given in the XRD and EDS analysis of Sb_2Se_3. Since selenium can condensate at the sample's surface, the detection of this phase is very common in the preparation of Sb_2Se_3 films [25]. The extra Raman peak detected at 295 cm^{-1} confirmed the existence of the Sb_2O_3 phase [25,27]. Raman measurement results revealed the existence of the Sb_2O_3 phase, although this phase was not detected by XRD, SEM, and EDS. There might be two reasons for this discrepancy. In Sb_2Se_3, the oxidation state of Sb is III which is the same as that in Sb_2O_3. In the present case, the oxygen can oxidize selenide to elemental selenium, which sublimes, while the oxygen itself is reduced to oxide, O^{2-} ions. This combines with the Sb (III) ions from Sb_2Se_3 and form Sb_2O_3. As a result, the air exposure after the annealing of the films converted traces of antimony selenide to antimony oxide. If Sb_2O_3 has an amorphous structure, it may not be seen in XRD analysis. Sb_2O_3 appears as small irregular shapes in white color on the film surface [4]. Since the Sb_2O_3 phase was not clearly seen in the surface image of the film taken by SEM (Fig. 3 (a)), the EDS analysis also gave a result that supports this situation. This can be ascribed to the presence of a partial oxygen-containing region on the surface of the film.

The other reason might be the laser heating effect of the Raman setup. When the high laser power density is used or the laser is dropped on the same point for a long time during the Raman measurement taken under air ambiance, the oxidation of antimony has been reported due to the laser-induced degradation of Sb_2Se_3 [25,27]. The findings of the Raman analysis allowed us to conclude that the Sb-Se-Sb vibrations were dominant in the Sb_2Se_3 thin film.

3.1.4. X-Ray photoelectron spectroscopy analysis of Sb_2Se_3 thin film

XPS measurement of the Sb_2Se_3 absorber on Mo-coated SLG substrate was performed to assist in the investigation of the composition and chemical bonding state of surface species. The instrumental binding energy calibration was carried out with respect to Ag $3d_{5/2}$ peak at 368.26eV [31]. Before the high-resolution XPS measurement of the absorber film, any sputtering process of the Sb_2Se_3 film surface by ion beam species was not applied. High-resolution spectra of C 1s, Sb *3d*, O 1s, Sb *4d*, and Se *3d* valence regions were measured in detail. CasaXPS software (Casa Software Ltd, UK) was used for the deconvolution process of these high-resolution spectra.

For possible charging effects, the binding energy scale of the spectra was calibrated using the C 1s peak arising from adventitious carbon. For this purpose, the C—C component of the C 1s spectrum which is present on all surfaces exposed to the ambient air with a binding energy of 284.6eV was used [31,32]. During the deconvolution process of the C 1s

region, it was considered a minor peak that corresponds to the inevitable formation of carbon-oxygen (C—O) bonds at the surface of samples that have been exposed to the atmosphere. Therefore, the C 1s valence region was fitted (Fig. 5 (a)) using the Shirley-type background for two sub-peaks with identical full width at half maximum (FWHM) values and the product of Gaussian and Lorentzian (GL) functions with around a 30% Gaussian ratio was used as a peak profile. Since the C—O peak is commonly detected at between 1.2 and 1.5eV higher binding energy position than the C—C peak, 1.2eV peak separation was applied between these peaks [33]. The Sb *3d*, Sb *4d*, and Se *3d* valence regions were deconvoluted using the sum of Gaussian and Lorentzian (SGL) functions with around a 30% Gaussian ratio while the product of Gaussian and Lorentzian (GL) functions with around a 30% Gaussian ratio was used for O 1s peaks. Due to the spin-orbit coupling, Sb and Se *3d* peaks and Sb *4d* peaks form as hybrids of $d_{5/2}$, and $d_{3/2}$. During the peak fitting analysis, the area of the $d_{5/2}$ components was constrained to be 1.5 times the area of the $d_{3/2}$ components. Also, the energy separation between the two peaks within a doublet and their FWHM values were fixed. Fig. 5 (b–d) shows a series of high-resolution XPS spectra for the constituent elements of Sb_2Se_3. The peak fitting results were listed in Table 1. Fig. 5 (b) shows the overlapping valence regions of Sb *3d* and O 1s. This region was fitted using two Sb *3d* doublets and two O 1s signals. The binding energy positions of Sb $3d_{5/2}$ (1) and Sb $3d_{3/2}$ (1) peaks agree well with the expected binding energies of Sb in the Sb_2Se_3 phase [24]. Furthermore, the separation of these sub-levels was 9.3eV which is in perfect agreement with that Sb is in oxidation state (III) in Sb_2Se_3. The doublet at higher binding energy (Sb $3d_{5/2}$ (2) and Sb $3d_{3/2}$ (2)) was attributed to Sb_2O_3. O 1s emission was fitted with two peaks. The peak observed at 531.84eV was attributed to O 1s in the Sb_2O_3 phase [34]. The second O 1s peak at the higher binding energy was attributed to an adventitious species related to carbon [35].

The Sb *4d* core level spectrum was deconvoluted best using two Sb *4d* doublets as given in Fig. 5 (c). The binding energy positions of Sb $4d_{5/2}$ (1) and Sb $4d_{3/2}$ (1) peaks were detected at 32.70eV and 33.90eV, respectively which was close to the reported binding energy value of Sb in the Sb_2Se_3 phase [36]. The second contribution of the Sb *4d* region was observed at 34.20eV and 35.40eV for Sb $4d_{5/2}$ (2) and Sb $4d_{3/2}$ (2), respectively, which was indicative of Sb in Sb_2O_3 [37–39].

For the Se *3d* region in Fig. 5 (d), two chemical species were identified. The peaks at 54.12 and 53.32eV corresponded to the Se $3d_{3/2}$ (1) and Se $3d_{5/2}$ (1) with the spin-orbit splitting of 0.8eV respectively, which demonstrates the Se^{2-} in the Sb_2Se_3 structure. In this valence region, to obtain a good fitting, it is necessary to consider a second contribution at the higher binding energy side. The position of the second contribution of Se $3d_{3/2}$ (2) and Se $3d_{5/2}$ (2) with the spin-orbit splitting of 0.8eV can be attributed to residual selenium [27,36]. XPS surface analysis exhibited the native oxide form of antimony as well as the Sb_2Se_3 phase.

3.1.5. Optical analysis of Sb_2Se_3 thin film

Fig. 6 shows the transmission of the Sb_2Se_3 thin film in the wavelength range from 200nm to 2600nm. Sb_2Se_3 absorber films are transparent materials in the infrared region. Therefore, their optical transmittance is observed higher in the near-infrared than in the visible region. However, from the transmission spectrum of Sb_2Se_3 film interference peaks were observed and the transmittance was only 50% at higher wavelengths. This means there is loss due to either scattering or reflection of light from the film. The optical band gap energy of Sb_2Se_3 thin film is determined from the formula $(\alpha h\nu)^n = K(h\nu - E_g)$ [5] where α is the absorption coefficient, K is a constant, $h\nu$ is the photon energy and E_g is the band gap energy. Here n assumes the values of 2 or 2/3 for allowed and forbidden direct transitions, respectively, and 1/2 and 1/3 for allowed and forbidden indirect transitions, respectively. Sb_2Se_3 can have allowed direct and indirect transitions. The optical band gap energy of Sb_2Se_3 thin film was extracted from $(\alpha h\vartheta)^n$ vs. $h\vartheta$ curve by drawing an extrapolation of the data point to the photon energy axis
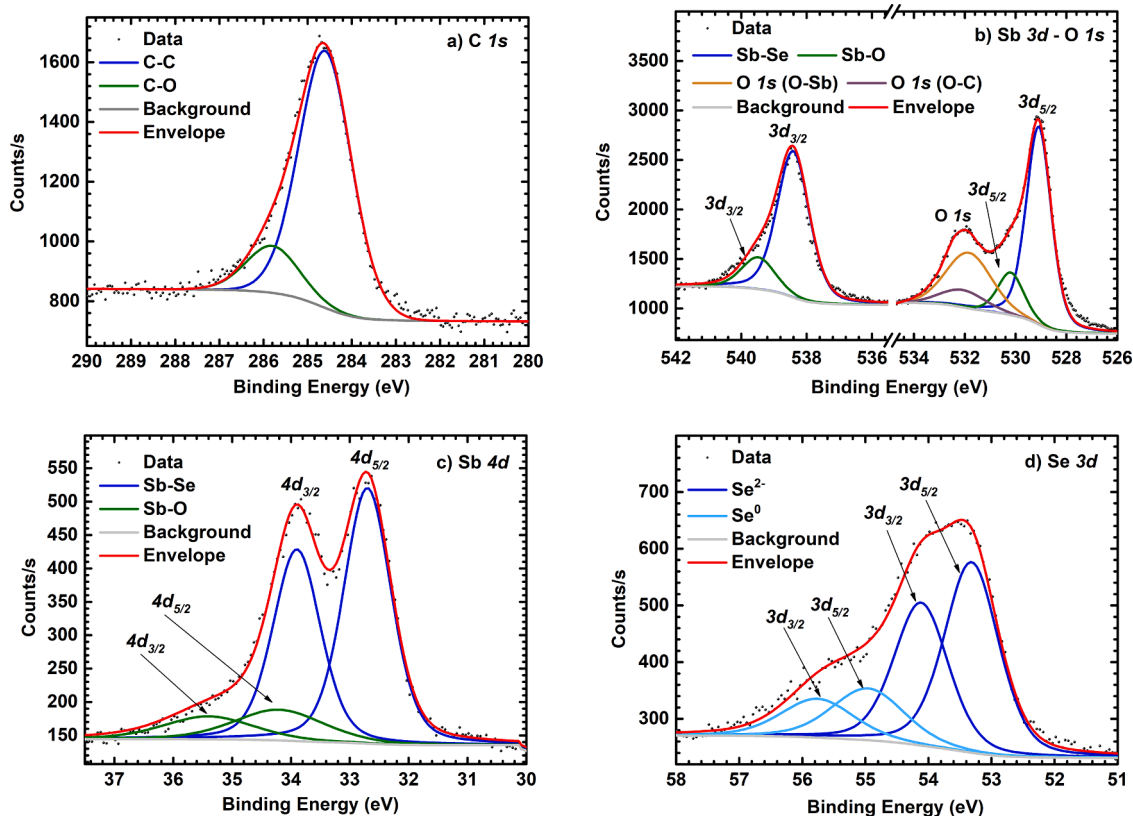
Fig. 5. High-resolution XPS peak fitting results of Sb$_2$Se$_3$ film on Mo-coated SLG substrate (a) C 1s, (b) Sb 3d-O 1s, (c) Sb 4d and (d) Se 3d valence regions.

Table 1
XPS peak fitting parameters of Sb 3d and 4d, O 1s, and Se 3d core levels.

Compound	core level	center (ev)	FWHM (eV)	Spin-Orbit Splitting (eV)	Line Shape
Sb-Se	Sb 3d$_{5/2}$	529.09	1.16	9.3	SLG (30)
	Sb 3d$_{3/2}$	538.39	1.16		SLG (30)
Sb-O	Sb 3d$_{5/2}$	530.19	1.20	9.3	SLG (30)
	Sb 3d$_{3/2}$	539.49	1.20		SLG (30)
O-Sb	O 1s	531.84	2.10		GL (30)
O—C	O 1s	532.07	2.10		GL (30)
Sb-Se	Sb 4d$_{5/2}$	32.70	0.95	1.2	SLG (30)
	Sb 4d$_{3/2}$	33.90	0.95		SLG (30)
Sb-O	Sb 4d$_{5/2}$	34.20	1.80	1.2	SLG (30)
	Sb 4d$_{3/2}$	35.40	1.80		SLG (30)
Sb-Se	Se 3d$_{5/2}$	53.32	1.01	0.8	SLG (30)
	Se 3d$_{3/2}$	54.12	1.01		SLG (30)
Se	Se 3d$_{5/2}$	54.96	1.35	0.8	SLG (30)
	Se 3d$_{3/2}$	55.76	1.35		SLG (30)

Fig. 6. Transmission spectra and optical bandgap of Sb$_2$Se$_3$ thin film.

fitting of absorption. The best straight-line fit of Tauch plot for allowed direct transition gave the band gap of 1.33eV in agreement with literature values [40].

3.1.6. Electrical analysis of Sb$_2$Se$_3$ thin film

The electrical property of the Sb$_2$Se$_3$ thin film was obtained from Hall measurements that occurred at room temperature. Van der Pauw method was used to determine the resistivity, carrier concentration, and mobility parameters of Sb$_2$Se$_3$ thin film and the results were listed in Table 2. Sb$_2$Se$_3$ thin film exhibited p-type conductivity behavior with 5.6×10^{-4} (Ω cm)$^{-1}$ conductivity value. Although the voids on the film surface, impurities, grain size, and grain boundaries change the

where $(\alpha h\vartheta)^n = 0$. Since the Tauc plot for allowed direct transition $((\alpha h\nu)^2 = 0)$ presented the linear behavior, the best straight line fit was found with allowed direct transition which was given as an inset of Fig. 6. For the n values of 1/2, 1/3, and 2/3 we did not observe a linear behavior, so band gap energy could not be extracted from the Tauch plot
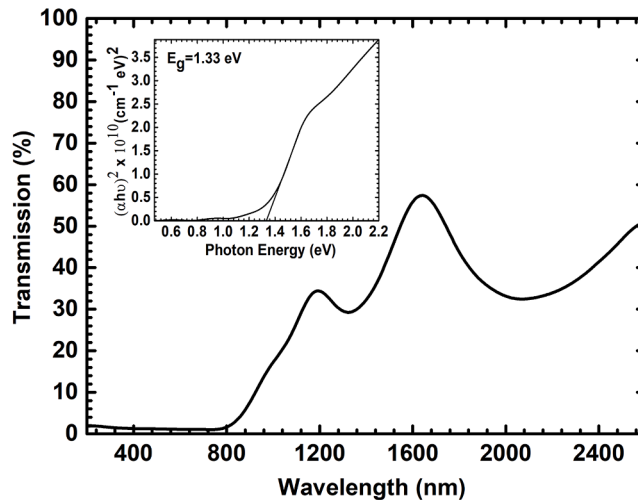
Table 2

The hall measurement results of Sb$_2$Se$_3$, CdS, and ZnS thin films.

Thin Film	Resistivity (Ω cm)	Carrier Concentration (cm^{-3})	Mobility (μ) (cm^{2}V^{-1}s^{-1})	Carrier Type
Sb$_2$Se$_3$	1794.9	85.6 *10^{13}	4.06	p
CdS	0.39	4.51 *10^{16}	352.33	n
ZnS	311	1.25 *10^{15}	16.08	n

resistivity value of the semiconductor, the resistivity value found was compatible with the literature [41]. The Sb$_2$Se$_3$ film exhibited a carrier concentration of 10^{13} cm^{-3} and 4.06 cm^2 V^{-1} s^{-1} mobility value close to the reported values [42].

3.2. Characterizations of CdS and ZnS thin films

3.2.1. Surface morphology and EDS analysis

The surface morphology of grown CdS thin film (in Fig. 7 (a)) had high coverage and few pinholes which have a direct influence on the film's optical and electrical properties. Since the ZnS thin film was deposited by the magnetron sputtering technique, it had a highly smooth surface. Therefore, a high-resolution surface image of ZnS could not be monitored by using SEM. Fig. 7 (b) demonstrates the surface image of the ZnS thin film that was taken during the EDS measurement. To obtain information about the stoichiometry of the films, the EDS analysis was carried out and the results were listed in Table 3 below. EDS result of the CdS thin film showed that the composition ratio of Cd and S elements (Cd/S) was 1.22 indicating the Cd-rich composition. Zn-Lα emission was used for determining the atomic percent of Zn. As the film was deposited on a soda lime glass substrate, there was interference with the Na-Kα
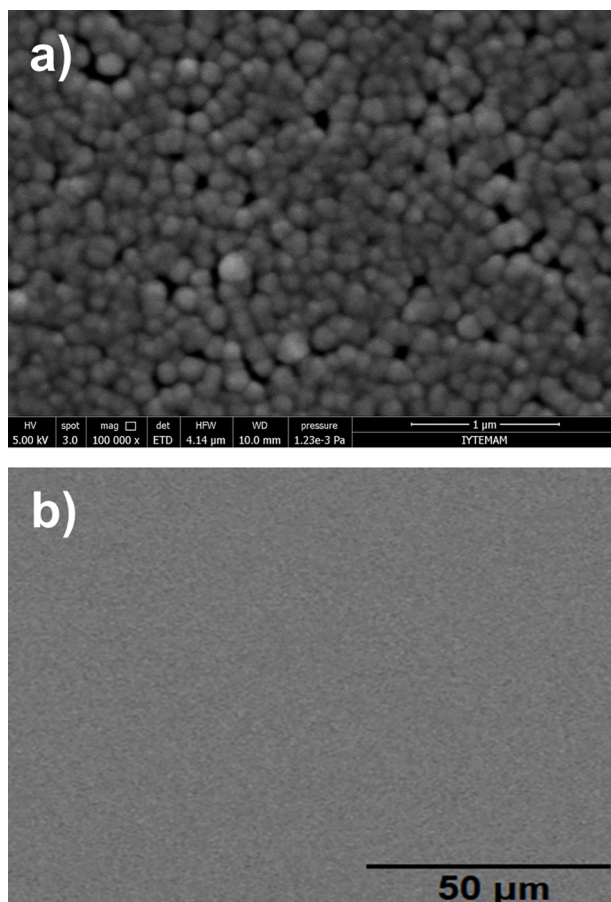
Table 3

EDS result of CdS and ZnS thin films deposited on SLG substrate.

Thin Film	CdS		ZnS				
Element	Cd	S	Zn	S	Na	Si	O
Atomic%	54.9	45.1	25.8	20.1	10.4	13.1	30.6

(1.041keV) and Zn-Lα (1.012keV) emissions. The Na and Zn concentrations were determined by Aztec software integrated with Oxford Instrument which was used for EDS measurement of ZnS thin film. The program deconvolutes the matched elements using standardless quantitative analysis. We noticed that the presence of Na, Si, and O originated from the soda lime glass substrate. The ZnS thin film exhibited that the composition ratio of Zn and S elements (Zn/S) was 1.28 indicating the Zn-rich composition.

3.2.2. Raman analysis

Figs. 8 (a) and (b) show the Raman spectra performed at 488nm excitation wavelengths of CdS and ZnS films, respectively. The Raman measurement of CdS exhibited three peaks which are the multi-overtones of longitudinal optical phonons (LO). The 1LO was the dominant Raman mode detected at 300 cm^{-1}. The first and second overtone modes (2LO and 3LO) were observed at approximately 600 cm^{-1} and 900 cm^{-1} [43].

The ZnS spectrum (Fig 8 (b)) shows peaks located around 212, 262, and 348 cm^{-1}. A peak at 560 cm^{-1} was from the underlying SLG

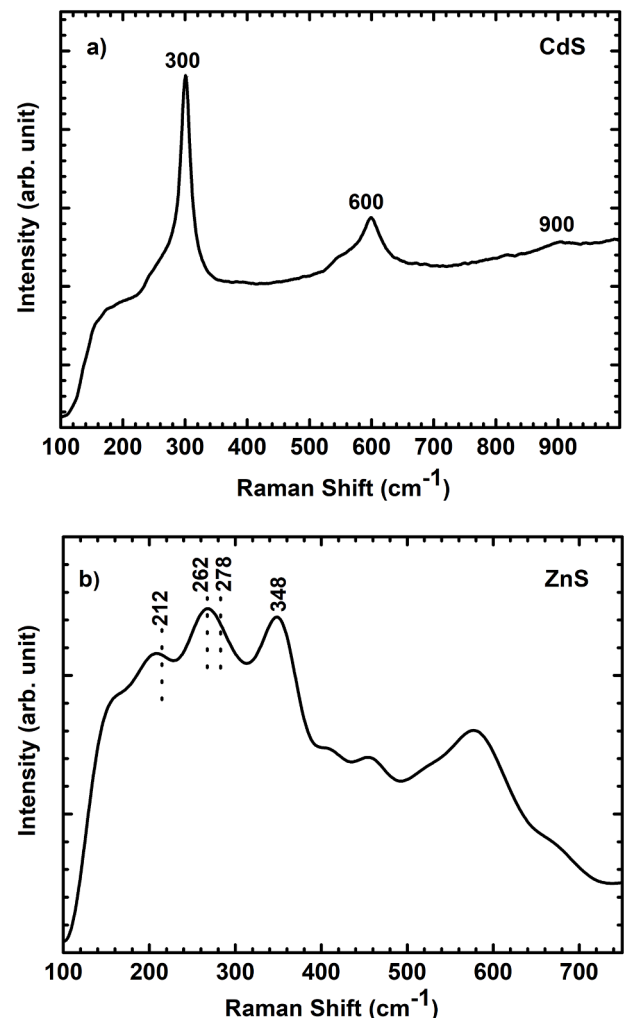**Fig. 7.** Surface morphology of (a) CdS and (b) ZnS thin films.

Fig. 8. Raman measurement of (a) CdS and (b) ZnS thin films.

substrate which is due to the high penetration depth of scattered photons in the samples (typically higher than one micrometer for 488nm excitation). Since the deposition was performed at a low temperature, the peak located at 348 cm^{-1} was assigned to the T_2 (LO) mode of zinc-blende (ZB) ZnS. The vibration line at 212 and 262 cm^{-1} were the second-order Raman modes of ZB ZnS and can be attributed to the two acoustic phonon combinations at W [44]. The broad band at 262 cm^{-1} mentioned above can also include the T_2 (TO) mode of ZB ZnS at 278 cm^{-1}.

3.2.3. Optical analysis

Optical properties of CdS and ZnS films were obtained by transmission measurements in the range of 200–2600nm at room temperature. In this study, ZnS, CdS, and Sb_2Se_3 films have been deposited on the same soda lime glass substrates. Therefore, readers should take the optical data with caution. The optical band gaps of the films for the allowed direct transition were derived by using the Tauc relation given in Section 3.1.5 above. The optical bandgap of the films was obtained from the extrapolation of the linear portion of the $(\alpha h\nu)^2$ curve to the axis of $(h\nu)$. The plot of $(\alpha h\nu)^2$ versus $(h\nu)$ was given as an inset of Fig. 9 (a) for the CdS and Fig. 9 (b) for the ZnS. As can be seen from Fig. 9 (a), the band gap energy of the CdS thin film was 2.43eV which is in harmony with the result that is given for CdS deposited by the CBD technique in the literature [45]. The band gap obtained for the ZnS as given in the inset of Fig. 9 (b) showed a close (E_g=3.62eV) to the reported value of magnetron sputtered ZnS thin film [46].
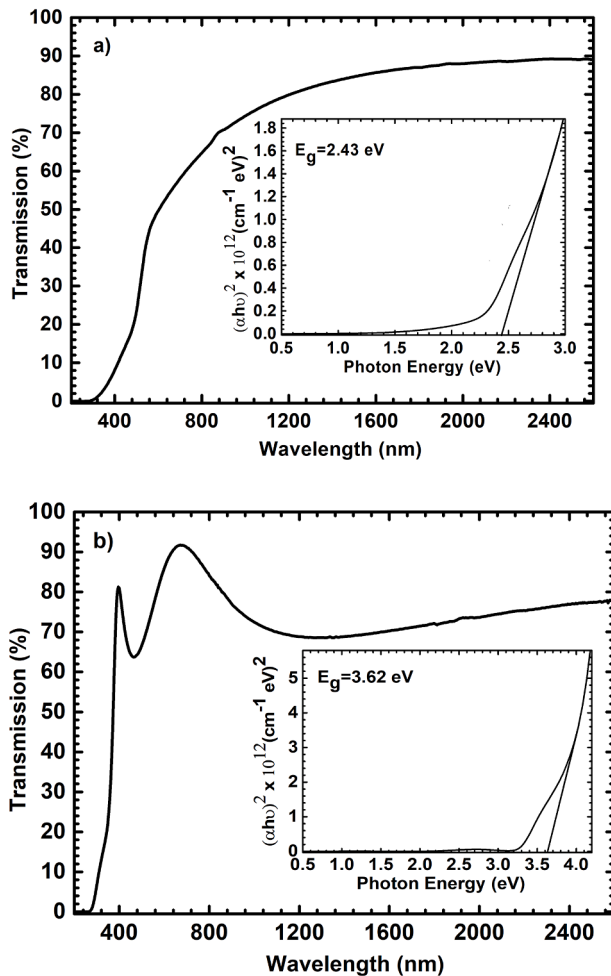
3.2.4. Electrical analysis

The electrical properties of the deposited CdS and ZnS thin films were inspected by the Hall Effect measurement at room temperature. The measured values of electrical resistivity, carrier concentration, and Hall mobility were listed in Table 2. Hall measurements of CdS and ZnS showed that both films had a negative Hall coefficient indicating n-type conductivity. The conductivity of CdS was calculated as 2.56 $(\Omega$ cm$)^{-1}$ where the Cd/S ratio is important for the conductivity of CdS. The excess of cadmium plays a donor role and causes the *n*-type conductivity [45, 47]. Such a high conductivity value was supported by the EDS result of CdS which showed excess Cd concentration. Due to the self-compensation effect created by sulfur vacancies, obtaining *p*-type CdS is very hard. The carrier concentration and the mobility parameters of CdS were compatible with the literature [48,49].

The conductivity value of ZnS thin film was calculated as 3.22 $^*10^{-3}$ $(\Omega$ cm$)^{-1}$. Since zinc excess is a donor-type defect, it contributes to the n-type conductivity [50]. The EDS result of the ZnS thin film supported such conductivity by showing a Zn-rich composition. The other electrical parameters such as resistivity, carrier concentration, and mobility were obtained in harmony with the reported values [51]. The characterizations of CdS and ZnS thin films displayed the required optoelectronic properties for photovoltaic applications.

3.3. Device characterization of Sb_2Se_3 solar cells

The representative cross-sectional SEM images of the devices were given in Fig. 10 (a) and (b). High-quality layer stacks with uniform, compact, well-adherent, and crack-free properties, which are useful for decreasing the recombination of charge carriers and eliminating the leakage current, were observed. Device performance of SLG/Mo/Sb_2Se_3/CdS/ZnS/ITO and SLG/Mo/Sb_2Se_3/CdS/ITO, which were

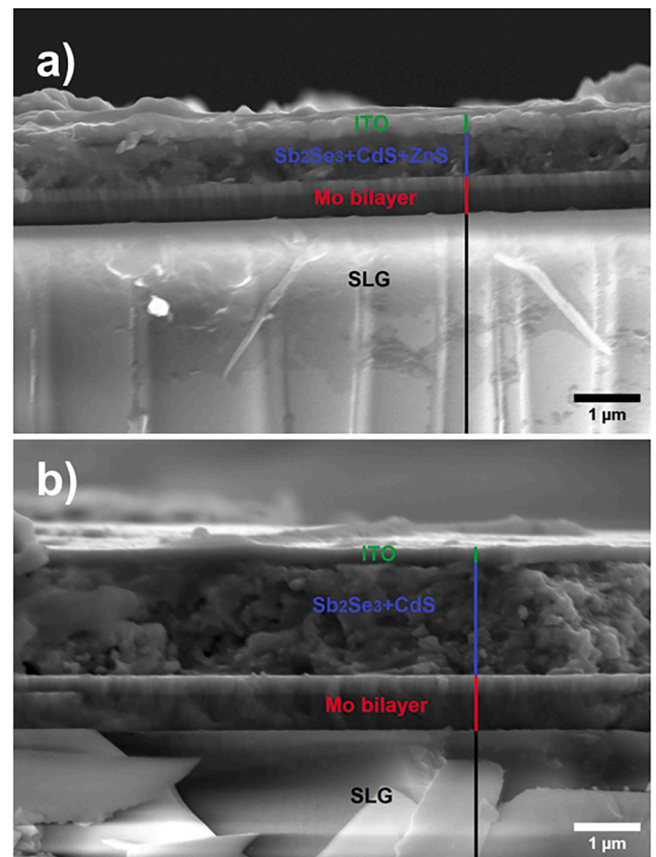**Fig. 9.** Transmission measurement of (a) CdS and (b) ZnS thin films.

Fig. 10. Cross-sectional SEM image of (a) SLG/Mo/Sb_2Se_3/CdS/ZnS/ITO and (b) SLG/Mo/Sb_2Se_3/CdS/ITO solar cell.

named with cell 1 and cell 2 respectively, were tested under simulated AM1.5G solar irradiation. Fig. 11 (a,b) shows the current density-voltage (J-V) curves of Sb_2Se_3-based solar cells. Cell 1 with a hybrid buffer layer offered a J_{SC} of 2.1mA/cm^2, a V_{OC} of 253mV, and a FF of 23.48% which resulted in a PCE of 0.13%. Cell 2 with a single buffer layer achieved better device performance with 3.93% PCE, V_{OC} of 305mV, J_{SC} of 29.6mA/cm^2, and FF of 43.04%. Sharp decrements in efficiency and J_{SC} and a slight decrement in V_{OC} of the device with the hybrid buffer layer may be attributed to an increment in the total thickness of the buffer layer with the hybrid form. This enhances the absorption of photons by the n-type buffer and reduces the generation of electron-hole pairs.

The other possible reason for the low performance of the Cell 1 might be due to the large lattice mismatch between the layers [52]. The lattice mismatch between CdS and ZnS layers is about 7% [53]. This large lattice mismatch may induce interfacial strain and may reduce the optical properties. Moreover, the valence band offset between ZnS and CdS interface is small and affected by strain state variation which results in the changing the transition from type I to type II [54]. The conduction band offset value between ZnS and CdS interface has quite strong strain dependence [54]. It might be considered that the strain dependency of interfacial properties of ZnS/CdS has a strong effect on cell performance. As a result, it seems that the hybrid buffer layer may limit the current flow through the device.

4. Conclusion

While the characteristics of Sb_2Se_3 thin films have been examined well so far, far less work has been done to explore the effects of CdS and the combination of CdS and ZnS buffer layers into a single solar cell. Therefore, in this study, we introduce a new device structure that has the potential to affect the Sb_2Se_3 solar cell device performance. Sb_2Se_3 thin film solar cells were studied with CdS/ZnS hybrid and a single CdS buffer layer. Firstly, the material properties of the Sb_2Se_3 absorber layer deposited on Mo-coated SLG substrate were examined. The Sb_2Se_3 layer showed good crystallinity, compact morphology, and nearly stoichiometric composition. XPS high-resolution spectra demonstrated the presence of Sb_2Se_3 film and also the Sb_2O_3 impurity phase, which was a result of exposure to air. Cross-section images of the fabricated devices showed a high-quality heterojunction interface with uniform, compact, well-adherent, and crack-free properties. Photoconversion efficiencies of 0.13% for SLG/Mo/Sb_2Se_3/CdS/ZnS/ITO and 3.93% for SLG/Mo/Sb_2Se_3/CdS/ITO cells were achieved. A sharp decrement in J_{SC} value was observed for the cell with hybrid buffer. The higher thickness of the hybrid buffer layer, inconvenient band alignment, and large lattice mismatch between the CdS/ZnS interface were considered possible reasons for this reduction.

This study confirms that the design of the device structure is essential in terms of band offset optimization at the interface to reduce the loss of photogenerated carriers in Sb_2Se_3 thin-film solar cells. Despite extensive theoretical investigations, still, there is no experimental result with satisfactory accuracy to determine the valence band and conduction band offset values of the CdS/ZnS interface value and the effect of hybrid buffer layer thickness on the performance of Sb_2Se_3 solar cells. Future work on this hybrid buffer layer should include the more in-depth performance of solar cells with a different thickness CdS/ZnS hybrid buffer layer.

CRediT authorship contribution statement

Ayten Cantas: Conceptualization, Formal analysis, Investigation, Project administration, Software, Supervision, Writing – original draft, Writing – review & editing. **S. Hazal Gundogan:** Conceptualization, Formal analysis, Investigation, Software. **Fulya Turkoglu:** Conceptualization, Formal analysis, Investigation, Software, Supervision, Writing – original draft, Writing – review & editing. **Hasan Koseoglu:**
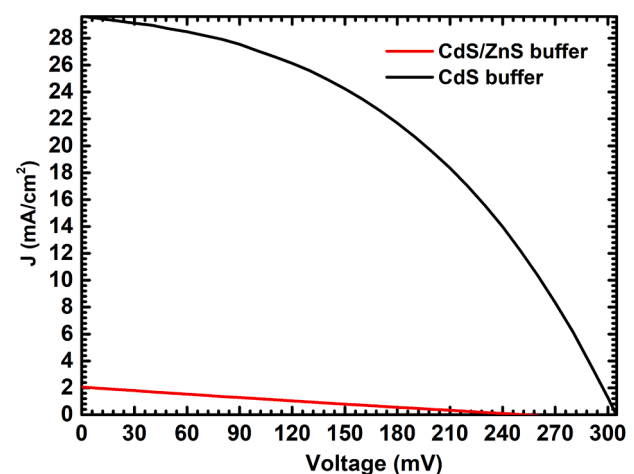

Fig. 11. J-V curves of Sb_2Se_3 devices.

Conceptualization, Formal analysis, Investigation, Software, Supervision, Writing – original draft, Writing – review & editing. **Gulnur Aygun:** Conceptualization, Formal analysis, Investigation, Software, Supervision, Writing – original draft, Writing – review & editing. **Lutfi Ozyuzer:** Conceptualization, Formal analysis, Investigation, Software, Supervision, Writing – original draft, Writing – original draft, Writing – review & editing.

Declaration of Competing Interest

The authors declare that they have no known competing financial interests or personal relationships that could have appeared to influence the work reported in this paper.

Data availability

The authors do not have permission to share data.

References

[1] M. Green, E. Dunlop, J. Hohl-Ebinger, M. Yoshita, N. Kopidakis, X. Hao, Solar cell efficiency tables (version 57), Prog. Photovolt. Res. Appl. 29 (1) (2021) 3–15, https://doi.org/10.1002/pip.3371.

[2] W. Wang, M.T. Winkler, O. Gunawan, T. Gokmen, T. Todorov, K. Zhu, Y.D.B. Mitzi, Device characteristics of CZTSSe thin-film solar cells with 12.6% efficiency, Adv. Energy Mater. 4 (7) (2014), 1301465, https://doi.org/10.1002/aenm.201301465.

[3] S.H. Gundogan, L. Ozyuzer, G. Aygun, A. Cantas, Magnetron sputtering deposition of sb$_2$se$_3$ thin films: physical property characterizations and its relevance for photovoltaics, in: Proceedings of the 2nd International Conference on Photovoltaic Science and Technologies (PVCon), IEEE, 2020, pp. 1–6, https://doi.org/10.1109/PVCon51547.2020.9757806.

[4] S.H. Gundogan, L. Ozyuzer, G. Aygun, A. Cantas, The effect of Ar gas flow rate on structure and optical properties of magnetron sputtered Sb_2Se_3 thin films for solar cells, in: Proceedings of the 2nd International Conference on Photovoltaic Science and Technologies (PVCon), IEEE, 2020, pp. 1–8, https://doi.org/10.1109/PVCon51547.2020.9757786.

[5] F. Turkoglu, M.E. Ekren, A. Cantas, K. Yakinci, H. Gundogan, H. Koseoglu, G. Aygun L. Ozyuzer, Structural and optical characteristics of antimony selenosulfide thin films prepared by a two-step method, J. Korean Phys. Soc. 81 (3) (2022) 278–284, https://doi.org/10.1007/s40042-022-00521-y.

[6] S. Messina, M.T.S. Nair, P.K. Nair, Antimony selenide absorber thin films in all chemically deposited solar cells, J. Electrochem. Soc. 156 (5) (2009) H327–H332, https://doi.org/10.1149/1.3089358.

[7] Y. Zhou, M. Leng, Z. Xia, J. Zhong, H. Song, X. Liu, B. Yang, J. Zhang, J. Chen, K. Zhou, Solution-processed antimony selenide heterojunction solar cells, Adv. Energy Mater. 4 (2014), 1301846, https://doi.org/10.1002/aenm.201301846.

[8] X. Wen, C. Chen, S. Lu, K. Li, R. Kondrotas, Y. Zhao, W. Chen, L. Gao, C. Wang, J. Zhang, N. Guangda, T. Jiang, Vapor transport deposition of antimony selenide thin film solar cells with 7.6% efficiency, Nat. Commun. 9 (2018) 1–10, https://doi.org/10.1038/s41467-018-04634-6.

[9] Z. Li, X. Liang, G. Li, H. Liu, H. Zhang, J. Guo, J. Chen, K. Shen, X. San, W. Yu, R.E. I. Schroop, Y. Mai, 9.2%-efficient core-shell structured antimony selenide nanorod array solar cells, Nat. Commun. 10 (2019) 1–9, https://doi.org/10.1038/s41467-018-07903-6.

[10] P. Büttner, F. Scheler, C. Pointer, D. Döhler, T. Yokosawa, E. Spiecker, P.P. Boix, E. R. Young, I. Mínguez-Bacho, J. Bachmann, ZnS ultrathin interfacial layers for optimizing carrier management in Sb2S3-based photovoltaics, ACS Appl. Mater. Interfaces 13 (10) (2021) 11861–11868, https://doi.org/10.1021/acsami.0c21365.

[11] Z. Yang, S. Wang, Y. Chen, Z. Zheng, Z. Chen, W. Xu, W. Liu, Y. Yang, J. Zhao, T. Chen, H. Zhu, Ultrafast self-trapping of photoexcited carriers sets the upper limit on antimony trisulfide photovoltaic devices, Nat. Commun. 10 (1) (2019) 1–8, https://doi.org/10.1038/s41467-019-12445-6.

[12] T.R. Rana, S. Kim, J. Kim, K. Kim, J.H. Yun, A Cd-reduced hybrid buffer layer of CdS/Zn(O, S) for environmentally friendly CIGS solar cells, Sustain. Energy Fuels 1 (9) (2017) 1981–1990, https://doi.org/10.1039/C7SE00348J.

[13] D.H. Shin, L. Larina, K.H. Yoon, B.T. Ahn, Fabrication of Cu(In,Ga)Se2 solar cell with ZnS/CdS double layer as an alternative buffer, Curr. Appl. Phys. 10 (2) (2010) S142–S145, https://doi.org/10.1016/j.cap.2009.11.019.

[14] J. Kim, H. Hiroi, T.K. Todorov, O. Gunawan, M. Kuwahara, T. Gokmen, D. Nair, M. Hopstaken, B. Shin, Y.S. Lee, W. Wang, H. Sugimoto, D.B. Mitzi, High-efficiency Cu2ZnSn(S,Se)4 solar cells by applying a double In2S3/CdS emitter, Adv. Mater. 26 (44) (2014) 7427–7431, https://doi.org/10.1002/adma.201402373.

[15] T. Liu, X. Liang, Y. Liu, X. Li, S. Wang, Y. Mai, Z. Li, Conduction band energy-level engineering for improving open-circuit voltage in antimony selenide nanorod array solar cells, Adv. Sci. 8 (16) (2021), 2100868, https://doi.org/10.1002/advs.202100868.

[16] J.S. Ho, S.C. Chang, J.J. Ho, W.T. Hsu, C.C. Chiang, S.Y. Tsai, S.S. Wang, C.K. Lin, C.C. Chou, C.H. Yeh, K.L. Wang, Improving the performance of solar cells with novel buffer structure by the chemical bath deposition technique, Mater. Sci. Semicond. Process. 59 (2017) 29–34, https://doi.org/10.1016/j.mssp.2016.09.044.

[17] K.K. Maurya, V.N. Singh, Enhancing the performance of a sb2se3-based solar cell by dual buffer layer, Sustainability 13 (21) (2021) 12320, https://doi.org/10.3390/su132112320.

[18] H.A. Mohamed, A.S. Mohamed, H.M. Ali, Theoretical study of ZnS/CdS bi-layer for thin-film CdTe solar cell, Mater. Res. Express 5 (5) (2018), 056411, https://doi.org/10.1088/2053-1591/aac5ae.

[19] S. Tripathi, P. Lohia, D.K. Dwivedi, Contribution to sustainable and environmentally friendly non-toxic CZTS solar cell with an innovative hybrid buffer layer, Sol. Energy 204 (2020) 748–760, https://doi.org/10.1016/j.solener.2020.05.033.

[20] R.L. Garris, L.M. Mansfield, B. Egaas, K. Ramanathan, Low-Cd CIGS solar cells made with a hybrid CdS/Zn(O,S) buffer layer, IEEE J. Photovolt. 7 (1) (2016) 281–285, https://doi.org/10.1109/JPHOTOV.2016.2617041.

[21] C. Yan, F. Liu, K. Sun, N. Song, J.A. Stride, F. Zhou, X. Hao, M. Green, Boosting the efficiency of pure sulfide CZTS solar cells using the In/Cd-based hybrid buffers, Sol. Energy Mater. Sol. Cells 144 (2016) 700–706, https://doi.org/10.1016/j.solmat.2015.10.019.

[22] F. Turkoglu, H. Koseoglu, A. Cantas, F.G. Akca, E. Meric, D.G. Buldu, M. Ozdemir, E. Tarhan, L. Ozyuzer, G. Aygun, Effect of defects and secondary phases in Cu2ZnSnS4 absorber material on the performance of Zn(O,S) buffered devices, Thin Solid Films 670 (2019) 6–16, https://doi.org/10.1016/j.tsf.2018.12.001.

[23] W.L. Bragg, The Crystalline State: Volume I, The Macmillan Company, New York, 1934.

[24] T. Ju, B. Koo, J.W. Jo, M.J. Ko, Enhanced photovoltaic performance of solution-processed Sb2Se3 thin film solar cells by optimizing device structure, Curr. Appl. Phys. 20 (2) (2020) 282–287, https://doi.org/10.1016/j.cap.2019.11.018.

[25] A. Shongalova, M.R. Correia, B. Vermang, J.M.V. Cunha, P.M.P. Salomé, P. A. Fernandes, On the identification of Sb2Se3 using Raman scattering, MRS Commun. 8 (3) (2018) 865–870, https://doi.org/10.1557/mrc.2018.94.

[26] N. Fleck, T. Hobson, C. Savory, J. Buckeridge, T. Veal, M.R. Correia, D.O. Scanlon, K. Durose, F. Jaeckel, Identifying Raman modes of Sb2Se3 and their symmetries using angle resolved polarised raman spectra, J. Mater. Chem. A 8 (2020) 8337–8344, https://doi.org/10.1039/D0TA01783C.

[27] C. Wang, S. Lu, S. Li, S. Wang, X. Lin, J. Zhang, R. Kondrotas, K. Li, C. Chen, J. Tang, Efficiency improvement of flexible Sb2Se3 solar cells with non-toxic buffer layer via interface engineering, Nano Energy 71 (2020), 104577, https://doi.org/10.1016/j.nanoen.2020.104577.

[28] K. Nagata, K. Ishibashi, Y. Miyamoto, Raman and infrared spectra of rhombohedral selenium, Jpn. J. Appl. Phys. 20 (3) (1981) 463–469, https://doi.org/10.1143/JJAP.20.463.

[29] B. Yang, D.J. Xue, M. Leng, J. Zhong, L. Wang, H. Song, Y. Zhou, J. Tang, Hydrazine solution processed Sb2S3, Sb2Se3 and Sb2(S1−xSex)3 film: molecular precursor identification, film fabrication and band gap tuning, Sci. Rep. 5 (1) (2015) 1–11, https://doi.org/10.1038/srep10978.

[30] V.S. Minaev, S.P. Timoshenkov, V.V. Kalugin, Structural and phase transformations in condensed selenium, J. Optoelectron. Adv. Mater. 7 (4) (2005) 1717–1741.

[31] P. Van der Heide, X-ray Photoelectron Spectroscopy: an Introduction to Principles and Practices, John Wiley & Sons Publishing Inc., New Jersey, 2011, p. 68.

[32] C.D. Wagner, Handbook of X-Ray Photoelectron spectroscopy: a Reference Book of Standard Data For Use in X-Ray Photoelectron Spectroscopy, Perkin-Elmer Publishing Inc., U.S.A., 1979, p. 9.

[33] T.R. Gengenbach, G.H. Major, M.R. Linford, C.D. Easton, Practical guides for x-ray photoelectron spectroscopy (XPS): interpreting the carbon 1s spectrum, J. Vac. Sci. 39 (1) (2021), 013204, https://doi.org/10.1116/6.0000682.

[34] C. Chen, Y. Zhao, S. Lu, K. Li, Y. Li, B. Yang, W. Chen, L. Wang, D. Li, H. Deng, F. Yi, J. Tang, Accelerated optimization of TiO2/Sb2Se3 thin film solar cells by high-throughput combinatorial approach, Adv. Energy Mater. 7 (20) (2017), 1700866, https://doi.org/10.1002/aenm.201700866.

[35] T.J. Whittles, T.D. Veal, C.N. Savory, A.W. Welch, F.W. de Souza Lucas, J. T. Gibbon, M. Birkett, R.J. Potter, D.O. Scanlon, A. Zakutayev, V.R. Dhanak, Core levels, band alignments, and valence-band states in CuSbS2 for solar cell applications, ACS Appl. Mater. Interfaces 9 (48) (2017) 41916–41926, https://doi.org/10.1021/acsami.7b14208.

[36] H. Shiel, O.S. Hutter, L.J. Phillips, M.A. Turkestani, V.R. Dhanak, T.D. Veal, K. Durose, J.D. Major, Chemical etching of Sb2Se3 solar cells: surface chemistry and back contact behaviour, J. Phys. Energy 1 (4) (2019), 045001, https://doi.org/10.1088/2515-7655/ab3c98.

[37] P. Singh, N. Ghorai, A. Thakur, H.N. Ghosh, Temperature-dependent ultrafast charge carrier dynamics in amorphous and crystalline Sb2Se3 thin films, J. Phys. Chem. C 125 (9) (2021) 5197–5206, https://doi.org/10.1021/acs.jpcc.0c11327.

[38] Y. Lechaux, A.B. Fadjie-Djomkam, M. Pastorek, X. Wallart, S. Bollaert, N. Wichmann, Study of the oxidation at the Al2O3/GaSb interface after NH4OH and HCl/(NH4)2S passivations and O2 plasma post atomic layer deposition process, J. Appl. Phys. 124 (17) (2018), 175302, https://doi.org/10.1063/1.5049571.

[39] S. McDonnell, D.M. Zhernokletov, A.P. Kirk, J. Kim, R.M. Wallace, In situ X-ray photoelectron spectroscopy characterization of Al2O3/GaSb interface evolution, Appl. Surf. Sci. 257 (20) (2011) 8747–8751, https://doi.org/10.1016/j.apsusc.2011.05.034.

[40] S.K. Kim, H.K. You, K.R. Yun, J.H. Kim, T.Y. Seong, Fabrication of high-responsivity Sb2Se3-based photodetectors through selenization process, Adv. Opt. Mater. 11 (7) (2023), 2202625, https://doi.org/10.1002/adom.202202625.

[41] A. Shongalova, M.R. Correia, J.P. Teixeira, J.P. Leitao, J.C. Gonzalez, S. Ranjbar, P. A. Fernandes, Growth of Sb2Se3 thin films by selenization of RF sputtered binary precursors, Sol. Energy Mater. Sol. Cells 187 (2018) 219–226, https://doi.org/10.1016/j.solmat.2018.08.003.

[42] C. Yuan, L. Zhang, W. Liu, C. Zhu, Rapid thermal process to fabricate Sb2Se3 thin film for solar cell application, Sol. Energy 137 (2016) 256–260, https://doi.org/10.1016/j.solener.2016.08.020.

[43] I.O. Oladeji, L. Chow, J.R. Liu, W.K. Chu, A.N.P. Bustamante, C. Fredricksen, A. F. Schulte, Comparative study of CdS thin films deposited by single, continuous, and multiple dip chemical processes, Thin Solid Films 359 (2) (2000) 154–159, https://doi.org/10.1016/S0040-6090(99)00747-6.

[44] Y.C. Cheng, C.Q. Jin, F. Gao, X.L. Wu, W. Zhong, S.H. Li, K. Paul, Raman scattering study of zinc blende and wurtzite ZnS, J. Appl. Phys. 106 (2009), 123505, https://doi.org/10.1063/1.3270401.

[45] F. Ouachtari, A. Rmili, B. Elidrissi, A. Bouaoud, H. Erguig, P. Elies, Influence of bath temperature, deposition time and S/Cd ratio on the structure, surface morphology, chemical composition and optical properties of CdS thin films elaborated by chemical bath deposition, J. Mod. Phys. 2 (2011) 1073–1082, https://doi.org/10.4236/jmp.2011.29131.

[46] I.D. Simandan, F. Sava, A.T. Buruiana, I. Burducea, N. Becherescu, C. Mihai, A. Velea, A.C. Galca, The effect of the deposition method on the structural and optical properties of ZnS thin films, Coatings 11 (9) (2021) 1064, https://doi.org/10.3390/coatings11091064.

[47] J.N. Alexander, S. Higashiya, D. Caskey, H. Efstathiadis, P. Haldar, Deposition and characterization of cadmium sulfide (CdS) by chemical bath deposition using an alternative chemistry cadmium precursor, Sol. Energy Mater. Sol. Cells 125 (2014) 47–53, https://doi.org/10.1016/j.solmat.2014.02.017.

[48] M. Fathy, A.E.H.B. Kashyout, S. Elyamny, G.D. Roston, A.A. Bishara, Effect of CdCl2 concentration and heat treatment on electrodeposited nano-crystalline CdS thin films from non-aqueous solution, Int. J. Electrochem. Sci. 9 (2014) 6155–6165.

[49] B.A. Ahmed, I.H. Shallal, F.I. mustafa AL-Attar, Physical properties of CdS/CdTe/CIGS thin films for solar cell application, J. Phys. Conf. Ser. 1032 (1) (2018), 012022, https://doi.org/10.1088/1742-6596/1032/1/012022.

[50] X.Y. Chu, X.N. Wang, J.H. Li, D. Yao, X. Fang, F. Fang, Z.P. Wei, X.H. Wang, Influence factors and mechanism of emission of ZnS: cu nanocrystals, Chin. Phys. B 24 (6) (2015), 067805, https://doi.org/10.1088/1674-1056/24/6/067805.

[51] C. Sabitha, I.H. Joe, K.D.A. Kumar, S. Valanarasu, Investigation of structural, optical and electrical properties of ZnS thin films prepared by nebulized spray pyrolysis for solar cell applications, Opt.Quantum Electron. 50 (153) (2018) 1–18, https://doi.org/10.1007/s11082-018-1418-z.

[52] R.B. Little, M.A. El-Sayed, G.W. Bryant, S. Burke, Formation of quantum-dot quantum well heteronanostructures with large lattice mismatch: znS/CdS/ZnS, J. Chem. Phys. 114 (4) (2001) 1813–1822, https://doi.org/10.1063/1.1333758.

[53] N. Pote, C. Phadnis, K. Sonawane, V. Sudarsan, S. Mahamuni, The impact of lattice strain on optical properties of CdS nanocrystals, Solid State Commun. 192 (2014) 6–9, https://doi.org/10.1016/j.ssc.2014.04.017.

[54] R. Said, A. Qteish, N. Meskini, The band lineups at highly strained ZnS/CdS and ZnSe/ZnTe interfaces: effects of the quadratic deformation potentials and the

relaxation of the semicore ᴅ-electrons, J. Phys. Condens. Matter 10 (39) (1998) 8703, https://doi.org/10.1088/0953-8984/10/39/009.